Journal of Data Acquisition and Processing
ISSN: 1004-9037
https://sjcjycl.cn/
DOI: 10.5281/zenodo.777582

AUTOMATED DETECTION OF GLAUCOMA IMAGES EMPLOYING CDR COMPUTATION AND BAYESIAN REGULARIZATION ALGORITHM

NirmalKaur[1]*, Prof.(Dr.) R.K.Bathla[2]
Research Scholar, Department of CSE, Desh Bhagat University,Mandi Gobindgarh, Punjab, India[1]
Professor, Department of CSE, Desh Bhagat University,Mandi Gobindgarh,, Punjab, India[2]
nirmalkaur@pbi.ac.in[1], prof.bathla@gmail.com[2]

Abstract
Medical image processing is a tool and technique for creating a visual image of inside of the body. The rapid advancement of digital imaging and computer vision has broadened the potential for the use of imaging technology in medicine. Image processing is especially useful in diagnostic medical systems. Reliable glaucoma detection in digital fundus images remains an open problem in biomedical image processing. Detection of glaucoma in the retinal fundus image is necessary to avoid loss of vision. The early detection of glaucoma and elevated inter ocular pressure is critically significant to arrest the progression of the irreversible disease. With the ocular degeneration of the retina and optic nerve, and other ailments such as high blood sugar levels, chronic blood pressure, thyroid imbalance and cataract, manual detection of glaucoma is often challenging leading to significant vision loss at the time of detection. Moreover, at low income group countries, medical costs also act as a deterrent for the early detection of the disease causing permanent vision loss. Hence, off late, research on the development of automated tools has been of paramount importance which can detect glaucoma with low false negative and false positive rates. In this paper, an image enhancement and feature extraction technique is developed which is subsequently used to train a deep neural network. Gray Level Co-occurrence matrix based features along with the cup to disc ratio have been used to train a Deep Bayes Net with regularization for automated detection of glaucoma. The performance of the proposed system has been evaluated in terms of the classification accuracy of the system.

Keywords: Fundus Image, Optic Disc, Biomedical image processing, Optic Disc detection, Bayesian Regularization, Cup to Disc Ratio (CDR).

1.Introduction

The retina is a layered tissue which is responsible for conversion of light signal into electrical signals for the brain to garner a sense of sight. Thus the retina is responsible for the creation of the optic images in the eye which are perceived by the brain as equivalent electrical signals giving a view of the outside world. In general, several physical ailments can result in the damage to the optic nerve and retinal function, among which hypertension, diabetes and other cardiovascular diseases are prominent [1].It has been found that glaucoma accounts for around 3 million cases of complete blindness and approximately 4 million cases resulting in visual impairment worldwide [2]. It is apprehended that the number of people affected by any sub-type of glaucoma will exceed a staggering 110 million by 2040 [3]. Although glaucoma can be found to affect people irrespective of their age, however higher chances of occurrence (in

between 1%-4%) is found among patients over the age of 40 [4] . The fundamental reason for the onset of glaucoma is the elevated level of intraocular pressure (IOP). Increased levels of IOP adversely affects the optic nerve causing irreversible damage, resulting in loss or impairment in vision depending on the magnitude of damage [5]. To save the vision of the individuals affected by glaucoma, the fundamental mechanism is to clinically reduce the levels of IOP. Clinical monotherapy or combination therapy, and in some cases surgical intervention may be required to reduce the levels of IOP to normal values [6]. While conventional medical practices have been prevalent in the diagnosis and subsequent treatment of glaucoma, recent advancements in the domain of artificial intelligence and machine learning have opened up new avenues for the early and accurate detection of glaucoma [7]. Automated computational tools can aid ophthalmologists to detect glaucoma at relatively early stages so as to minimize the damage to optic nerve and hence reduce visual impairments. Moreover, it world form the basis for a strong second opinion. It can be particularly useful in areas which lack advanced medical facilities, typically common in remote areas of low income group countries [8]. Several automated techniques have been developed and explored based on the statistical analysis of the fundus image. The basic approach is to pre-process the image to remove the effects of noise and disturbance followed by feature extraction and classification using a machine learning based classifier [9]-[10]. The machine learning based classified is trained with images of two categories viz. affected by glaucoma and unaffected with glaucoma. The classifier tries to identify the patterns in the data and hence classify any new sample of the fundus image as glaucoma positive or negative [11].

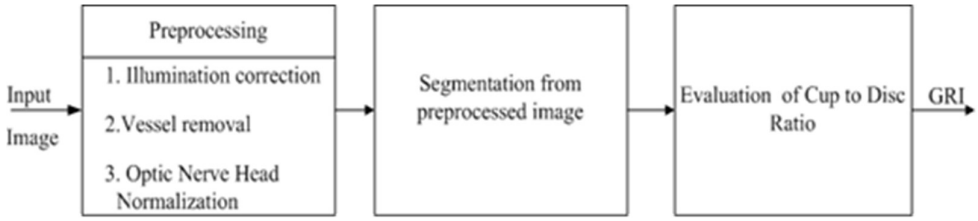

Fig. 1.Processing pipeline steps: (i) Preprocessing of input images for eliminating disease independent variations, (ii) Segmentation of preprocessed image and (iii) Classification based on CDR for generating Glaucoma Risk Index (GRI)

The fundus images obtained from fundus imaging need to be processed and analysed to extract critical features for the decision on presence or absence of glaucoma or pre-glaucoma like symptoms [12]-[13]. Due to the occurrence of noise and disturbance effects while capturing, retrieving, processing and storing the images, the final classification may be prone to errors [14]. This necessitates case sensitive noise removal and image restoration techniques which can enhance the quality of the images under interest so as to facilitate feature extraction and pattern recognition [15]. This paper presents an combined approach for image enhancement and feature extraction pertaining to fundus images which would facilitate automated detection of glaucoma [16].

2.Theoretical Background and Existing Work

The retina is a layered tissue which is responsible for conversion of light signal into electrical signals for the brain to garner a sense of sight [17]. Thus the retina is responsible for the creation of the optic images in the eye which are perceived by the brain as equivalent electrical signals giving a view of the outside world. In general, several physical ailments can result in the damage to the optic nerve and retinal function, among which hypertension, diabetes and other cardiovascular diseases are prominent [18]-[19]. A significant part of the above causes is diabetic retinopathy which is caused by excess blood sugar levels in the blood streams causing irreversible damage to the heart, lungs, kidneys and eyes[20]. Typically, patients suffering from type-2 diabetes often suffer from diabetic retinopathy and this causes serious damage to the peripheral vision in humans. In developed countries, glaucoma is also termed as the silent snatcher of eyesight, which can only be arrested but not reversed making its early and accurate detection extremely crucial [21]. With sedentary lifestyles, poor eating habits, depleting nutritional values in food intake, these diseases are often interconnected and are also progressing fast worldwide [22]. A typical retinal image is depicted in figure 2 which consists of blood vessels, optic disc (OD), Optic Cup (OC) and the macular region.

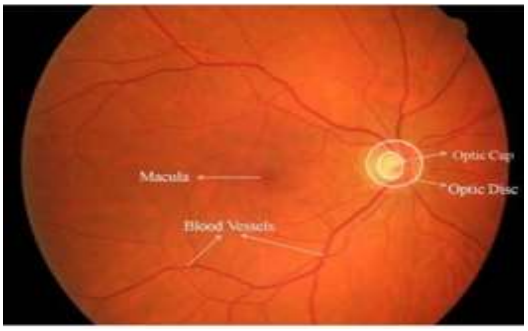

Figure 2A typical fundus image for detection of glaucoma
(Source: https://www.aao.org/eye-health)

The blood vessels perform the task of supplying blood to the entire retinal area by spreading across the length and breadth of the retinal region [23]. The damage to the optic nerves and vessels are caused by excessive blood pressure to the vessels primarily caused by [24]:

1) Hyper tension
2) High blood glucose levels.

The additional pressure of the blood modifies the elasticity of the blood vessels and also their texture resulting in macular degradation [25]-[26]. Often this can be perceived as flashes and floaters, loss of peripheral vision and erroneous perception of depth.

The pivotal aspect in the detection and treatment of glaucoma is the process of retinal imaging which is 2-Dimensional projection of the 3-Dimensional retinal image on an imaging plane. Such images are also termed as fundus images [27]. The different retinal imaging techniques commonly employed are [28]-[30]:

1.1 Fundus Photography:

In the case of fundus photography, a wideband (in visible spectrum) reflected light representation is captured which constitutes the fundus image.

1.2 Color Fundus Photography:

This is a modified version of the fundus photography wherein a three channel representation of the reflected light is images in terms of the R-G-B values in the waveband.

1.3 Stereo Fundus Photography:

This imaging technique comprises of combining light waves form two or more visual angles to garner information regarding the depth of resolution. Lower resolution results in the patients impairment to distinguish between different objects and considering them as a composite object.

1.4 Hyper Spectral Imaging:

This technique consist of capturing a composite image created from light reflections from specific wavelengths. The intensity response of different wavelengths represents the capturing capability of the retina to respond to different colours.

1.5 Scanning LASER Ophthalmoscope (SLO):

The SLO technique analyses a temporal pattern of the reflection intensities to a fixed LASER. The process is based on the phenomenon of back scattering causing back scattering of light from the LASER source. A modified version of the technique constitutes Laser Scanning Tomography (SLT) which tries to gather multi-wavelength resolution by changing the wavelength of the Laser source.

1.6 Fluorescein angiography (FA):

This procedure consists of injecting a fluorescent dye into the blood which results in clear photography of the blood vessels in the eye. This type of imaging is very useful for diabetic retinopathy and can help to assess the amount of proliferation [31].

There are other reasons of vision loss among patients which are typically age related macular degradation, diabetic retinopathy, cardio vascular diseases affecting the vision and cataract. While glaucoma is not necessarily an outcome of the aforesaid health problems, yet studies show a dependence and close correlation among these common ailments and the onset of glaucoma among patients [32].

Table 1Brief Review of Previous Work

Authors	Technique	Advantages	Limitations
Memari et al. [1]	Fuzzy C-means clustering.	Vessel center lines clearly enhanced with labelled Fuzzy training.	Saturation of performance after which adding training data doesn't improve performance.
Mendonca et al. [2]	Multi-scale morphological enhancement technique	Vessel center lines were clearly enhanced	Not suitable for low resolution retinal images
Perez et al. [3]	Morphological Reconstruction.	Low complexity.	Image inpainting not incorporated after segmentation of vessel structures.
Marin et al. [4]	Gray level and moment feature based supervised classifier	Background enhancement, with high contrast difference between vessel and Background.	Relatively low accuracy and sensitivity, due to computation of moment features only.

Fraz et al. [5]	Ensemble classifier	Suitable for both low and high resolution retinal images	Relatively higher computational complexity.
Xiao et al. [6]	Bayesian classifier	Clear segmentation of vessels from the background pixels	Relatively low sensitivity and saturation of performance with adding data to training set.
Bansal et al. [7]	Fuzzy Classifier	Relatively high accuracy.	Relative high computational complexity with increasing features and performance saturation for less number of features.
Budai et al. [8]	Frangi algorithm	Low computational complexity.	Relatively low accuracy owing to lesser number of features extracted.
Wong et al. [9]	Seeded mode tracking approach with feature computation.	Relatively high accuracy.	Not applicable for low resolution images.
Khawaja et al. [10]	Directional Multiscale Line Detectors	Robust multi-variate classifier.	Relatively low accuracy
Islam et al. [11]	Deep-learning-based approach	Relatively high accuracy with low and high level features extracted through hidden layers of Deep Neural Network.	Relatively high computational complexity.
Ceccon et al. [12]	Naïve Bayes Classifier	Probabilistic approach robust for overlapping features.	Background enhancement and noise removal not explored.

3.Methods

With the availability of exhaustive digital data records in the medical field coupled with the increasing processing powers of computational algorithms, automated detection of glaucoma has gained prominence. For accurate classification of glaucoma images, it is fundamentally important to pre-process the images prior to actual classification [33]. In this paper, each of the sub-processes employed for image enhancement and subsequent feature extraction are explained in this section.

RGB to Grayscale Conversion: Typically, acquired fundus images are contain three color channels which are Red, Green and Blue (RGB channels). Analyzing high resolution RGB images requires much higher compute power as compared to analyzing images with a single intensity variable as in the case of grayscale images (with grayscale or intensity variable). The luminosity algorithm for RGB to grayscale conversion is done based on the following relation [16]:

$$\boldsymbol{I_{GS} = 0.28R + 0.5G + 0.09B} \quad \textbf{(1)}$$

Here,

I_{GS}corresponds the pixel value of the grayscale image.
Rcorresponds to the red component of the pixel.
Gcorresponds to the green component of the pixel.
Bcorresponds to the blue component of the pixel.

$$\boldsymbol{G(x,y) = ke^{\frac{-(x^2+y^2)}{s^2}}} \quad \textbf{(2)}$$

Here,
$\boldsymbol{G(x,y)}$is the Gaussian Kernel.
$\boldsymbol{k}$represents the normalizing co-efficient.

$\boldsymbol{s}$represents the scaling co-efficient of the kernel.
$(\boldsymbol{x}, \boldsymbol{y})$represent the spatial co-ordinates.

The reflection co-efficient value $I_R(x, y)$ is estimated by convolving the input image and the Gaussian function in the periphery bound the contour $'C'$. The weight co-efficient $\boldsymbol{w}$is updated throughout the contour for the number of scales $\boldsymbol{i} = \boldsymbol{1}:\boldsymbol{n}$. Further a linear transform to adjust the objectively captured image I and the corrected image I_C is given by [36]:

$$\boldsymbol{I_C = \beta_1 log_e I + \beta_2} \quad \textbf{(3)}$$

Here,

IandI_C corresponds to the physically captured and illumination corrected images respectively.
$\boldsymbol{\beta_1}$ $\boldsymbol{and}$ $\boldsymbol{\beta_2}$are correction constants.

The next process is the computation of the two-dimensional spatial correlation given by [37]-[39]:

$$\boldsymbol{C(x, y) = \frac{I(x,y) - I_C(x,y)}{I(x,y) - I_B(x,y)} . k} \quad \textbf{(4)}$$

Here,
Crepresents the correlation.
$k$denotes the normalizing co-efficient.
Idenotes the original image
$I_C$denotes image correlation
$I_B$denotes image background

The histogram normalization is computed based on the difference in the eigen values of the original and corrected image given by:

$$\boldsymbol{|kI - I_C|} \quad \textbf{(5)}$$

The covariance of the image can be computed as:

$$\boldsymbol{C_V = \frac{mean\,[I(x,y) - I_C(x,y)]}{|kI - I_C|}} \quad \textbf{(6)}$$

Here,
$mean$denotes the average operation.

The subsequent process is to add the product of the weight matrix and normalized co-variance co-efficient to the originally corrected image given by:

$$\boldsymbol{N_I = I(x, y) - I_C\{(x, y)\} + mean(w * C_V)]} \quad \textbf{(7)}$$

Here,
$N_I$denotes the normalized image.
$w$denotes the correlation weights.

Segmentation of Optical Cup and Disc:

A critical attribute to differentiate among glaucoma positive and negative images is the cup to disc ratio (CDR) [40]. The vertical cup to disc ratio (CDR) is a widely accepted clinical parameter that is used for optic nerve health (ONH) assessment. The CDR value of aglaucoma patient is relatively larger than the normal one. The DDR value is computed as [41]:

$$\boldsymbol{CDR = \frac{radius\ of\ cup\ from\ origin}{radius\ of\ disc\ from\ origin}} \quad \textbf{(8)}$$

The CDR can be computed by first segmenting the cup and disc regions of the retinal fundus image and subsequently estimating the cup and disc diameters. One of the major challenges in this domain is to attain low computational complexity for the system and hence a Euclidean distance based interpolation method is adopted in this method. For this

purpose, the pixel correlation is computed for a patch of images wherein the inpainting is to be applied and is expressed as:

$$\boldsymbol{C_{patch} = \|P_T - P_C\|^2} \quad \textbf{(9)}$$

Here,

$\boldsymbol{C_{patch}}$denotes the squared Euclidean norm for the patch.
$\boldsymbol{P_T}$denotes the target patch.
$\boldsymbol{P_T}$denotes the candidate patch.

Next, the pixels are weighed averages of the existing pixels satisfying the interpolation condition:

$$\boldsymbol{Z = argmin(P_T - P_C) \ll mean|P_S|} \quad \textbf{(10)}$$

Here,
$Z$is the minimum interpolated difference co-efficient.
$\boldsymbol{mean|P_S|}$is the average pixel magnitude of the patch.

The patch based approach for segmenting the cup and disc are effective as there are overlapping boundaries in the fundus images and clear boundary identification is infeasible computationally. The cup and disc patches are identified based on the sum of average and consecutive standard deviations given by:

$$\boldsymbol{\mu + \frac{\sigma^2}{(\sigma+1)^2}} \quad \textbf{(11)}$$

Here,
$\mu$is the average pixel values.
$\sigma$is the standard deviation.

This type of interpolation allows cup and disc estimation of both the mean pixel values as well as the extremities based on the standard deviations. This serves as a more robust technique compared to the conventional averaging approach. To identify the patch, the radial gradient of the fundus image is to be computed given by:

$$\boldsymbol{g_r = \frac{\partial}{\partial r}\oint_{r,x_0,y_0}^{r,x_f,y_f} \frac{I(x,y)}{2\pi r} ds|} \quad \textbf{(12)}$$

Here,
(x, y)denote image pixels
$r$denotes radius
$g_r$denotes radial gradient

Noise Removal: The next approach is the removal of the inherent noise effects in the image whose occurrence may the have following reasons [19].

1) Addition of electronic noise in the image due to the use of amplifiers in the sensing device which is also termed as white or Gaussian noise.
2) The abrupt change or spikes in the analog to digital converters sued in the circuity of the fundus image causing salt and pepper noise patterns.
3) The multiplicative noise effect due to the inconsistent gain of the adaptive gain control (AGC) circuity used for capturing or retrieving the fundus image [20].
4) The lack of pixels while capturing the image resulting in frequency mean valued interpolations in the reconstructed image causing Poisson image [21].

$$\boldsymbol{CWT(x,s,\delta) = s^{\frac{1}{2}} \int_{-\infty}^{\infty} x(t)\, \emptyset^*(\frac{t-s}{\delta})dt} \quad \textbf{(13)}$$

Where,
$s, \delta \in R$represent the scaling (dilation) and shifting (translation) constants constrained to the condition $\delta \neq 0$.
$\emptyset^*$is the Wavelet Family or Mother Wavelet
$t$is the time variable
$x(t)$is the time domain data.

For implementing the wavelet transform on the image dataset, the sampled version of the continuous wavelet transform yields the discrete wavelet transform given by:

$$\boldsymbol{DWT(x,m,n) = \delta_0^{m\frac{-1}{2}} \sum_i x(i) \emptyset^* \left[\frac{n - is_0^m}{s_0^m}\right]} \quad \textbf{(14)}$$

Where,
$x(i)$is the discrete $k \times 1$ vector.
$s_0^m$is the discrete scaling constant.
$is_0^m$is the discrete shifting constant.

The discrete wavelet transform yields two distinct low and high pass values based on the number of levels of decomposition and wavelet family given by the approximate co-efficient (CA) and detailed co-efficient (CD). The approximate co-efficient values are typically the low pass values containing the maximum information content of the image while the detailed co-efficient values account for the noisy spectral part[45]. Retaining the low pass co-efficients and recursively discarding the high pass co-efficients allows to de-noise the image [46]. The choice of the wavelet family impacts the estimation of the noise gradient vector given by:

$$\boldsymbol{G_N = k\frac{\nabla I}{\nabla I_F}} \quad \textbf{(15)}$$

The value of the second order normalizing gradient as a function of spatial co-ordinates is given by:

$$\boldsymbol{q(x,y) = \sqrt{\frac{c_1(\nabla I/_{I_F})^2 + c_2(\nabla^2 I/_{I_F})^2}{(1 + c_3(\nabla^2 I/_{I_F})^2}}} \quad \textbf{(16)}$$

Here,
Idenotes the original image.
$I_F$denotes the fused image after normalization.
$\boldsymbol{G_N}$denotes the normalizing gradient.
∇represents the gradient.
∇^2represents the Laplacian.

Feature Extraction: After the pre-processing and enhancement of the image is performed, the next process is the computation of statistical and texture based features from the image dataset. In recent literature it is found that a combination of both statistical and texture features are effective for classification problems. The features computed in the paper are [47]-[48]:

$$\boldsymbol{Mean = \frac{1}{N}\sum_{i,j}^{N} f_{i,j}} \quad \textbf{(17)}$$

$$\boldsymbol{s.d. = \sqrt{\frac{1}{N}\sum_{i,j}^{N}(f_{i,j} - mean)^2}} \quad \textbf{(18)}$$

$$\boldsymbol{v = \frac{1}{N}\sum_{i,j}^{N}(f_{i,j} - mean)^2} \quad \textbf{(19)}$$

$$\boldsymbol{skewness = \sqrt[3]{\frac{1}{N}\sum_{i,j}^{N}(f_{i,j} - mean)^3}} \quad \textbf{(20)}$$

$$\boldsymbol{Kurtosis = E[\left(\frac{X - mean}{s.d.}\right)^4]} \quad \textbf{(21)}$$

$$\boldsymbol{rms} = \frac{\mathbf{1}}{\boldsymbol{n}}\sqrt{\sum_{\boldsymbol{i=1}}^{\boldsymbol{n}} \boldsymbol{p_i^2}} \quad \textbf{(22)}$$

$$\boldsymbol{Energy} = \sum_{\boldsymbol{i,j}}^{\boldsymbol{N}} \left|\boldsymbol{p_{i,j}}\right|^{\mathbf{2}} \quad \textbf{(23)}$$

$$\boldsymbol{Contrast} = \sqrt{\frac{\mathbf{1}}{\boldsymbol{mn}}\sum_{\boldsymbol{i,j}}^{\boldsymbol{m,n}}[\boldsymbol{X(i,j)} - \boldsymbol{mean}\{\boldsymbol{X(i,j)}\}]^{\mathbf{2}}} \quad \textbf{(24)}$$

$$\boldsymbol{Corr_{2D}} = \sum_{\boldsymbol{i,j}}^{\boldsymbol{M,N}} \frac{\boldsymbol{(i-m_x)(j-m_j)P_{x,y}}}{\boldsymbol{sd_x sd_y}} \quad \textbf{(25)}$$

$$\boldsymbol{E} = -\boldsymbol{P}[\boldsymbol{I_{x,y}}]\boldsymbol{log_2}[[\boldsymbol{I_{x,y}}] \quad \textbf{(26)}$$

$$\boldsymbol{H} = \sum_{\boldsymbol{i,j}}^{\boldsymbol{M,N}} \frac{\boldsymbol{P_{i,j}}}{\mathbf{1}-\boldsymbol{(i-j)^2}} \quad \textbf{(27)}$$

$$\boldsymbol{smoothness} = \frac{\boldsymbol{a}}{\mathbf{1}+\boldsymbol{a}} \quad \textbf{(28)}$$

Here,
$f_{i,j}$corresponds to the i[th] colour component for pixel j
$mean\ (m)$ denotes the average of the statistical features.
$s.d.$denotes standard deviation
$v$denotes the variance
$n$denotes the number of pixels
$p$denotes the pixel value.
Pdenotes the probability of occurrence of pixel I w.r.t. pixel j.
$Corr_{2D}$denotes 2-dimensional correlation
M & Ndenote the number pf pixels along x & y
$m_x$denotes mean along x
$m_y$denotes mean along y
sd_xdenotes standard deviation along x
sd_ydenotes standard deviation along y

Feature extraction serves as a serves the purpose of extracting empirical statistical information from raw data. The feature values defined serve as the parameters based on which any automated tool would classify a new fundus image sample as a positive or negative case of glaucoma. The veracity of the feature extraction process can be checked based on the correlation among the extracted features for a large dataset or a subset of the dataset. While individual image samples may exhibit divergences, yet the magnitude of such divergences in generally bound. Hence, a correlation among the extracted features would testify for the correctness of the feature extraction process and its applicability for pattern recognition by any automated classifier.
The choice of suitable feature descriptor as well as the classification model is a major concern with automated techniques for glaucoma detection. Generic deep learning based models such as convolutional neural networks (CNNs), Region based CNNs i.e. RCNNs etc. use a gradient-based algorithms to tune the model parameters. Their generalization performance strongly relies on the number of training samples used and they tend to perform poorly with limited training samples. Further, these methods consider the classification error to tune the parameters [49]. It is worth mentioning that these models may not always generate the best feature descriptors since their training stops after reaching a high threshold value. Such performance on the training set does not guarantee better performance on unknown clinical data. The CDR value alone doesn't render high accuracy of classification though. The combination of the CDR value along with the statistical features (handpicked) result in relatively higher accuracy.
Design of Automated Classifier: The design of the automated classifier is critically important as the accuracy of classification critically depends on the design of the classifier. Generally, positive and negative fundus images show overlapping CDR and feature values. Hence a probabilistic approach is often effective. As fundus image processing is practically carried out in hospitals to medical facilities, hence deep learning algorithms which need large computational resources may render infeasibility to even a novel and accurate approach. This leads to a natural inclination towards the Bayesian Regularization algorithm [50].

the labelled data vector $Tr = [f_1 \dots \dots \dots . f_{12}]_{no\ of\ images}$ is fed to the bayesian regularized ann. the brann is chosen as it is an effective classifier. it works on the principle of Baye's theorem of conditional probability. After the BRANN is trained, in the testing phase, the BRANN calculates the probability of an element to belong to a particular category. For a multi-class decision, the higher probability of a particular class decides the category of the data. In case of the BRANN tries to find out the probability of an image to be actually positive based on the probability before passing the judgement [51]For this, the important assumption which the BRANN makes is that of the accuracy of the classifier. This is dependent on the training accuracy which is available to the classier (on completion of training) and the number of positive images in the dataset (already available to the classifier as the dataset provided by the user, which the classifier assumes to be true). The same logic applies to the negative fundus images.

The weight of the network are to be chosen in such a way that it maximizes the conditional probability of a data belonging to a particular class. The weight updating rule is given by:

$$\boldsymbol{w_{k+1} = w_k - \left[J_k J_k^T + \mu I\right]^{-1} J_k^T e_k} \quad \textbf{(29)}$$

Here,
w_k is weight of present iteration k
w_{k+1} is weight of next iteration (k+1)
e_k is error of present iteration
J_k is the Jacobian Matrix which contains 2nd order derivatives of errors w.r.t. weights i.e. $\frac{\partial^2 e}{\partial_w^2}$
J_k^T is the transpose of the Jacobian Matrix
I is an identity matrix
μ is the step size or combination co-efficient which is the amount by which the weight changes in each iteration

Implementing the BR algorithm needs a clear understanding of the Bayesian Theorem for conditional probability stated as:

$$\boldsymbol{Prob\left(\frac{M}{N}\right) = \frac{Prob\left(\frac{N}{M}\right).Prob\,(M)}{Prob\,(N)}} \quad \textbf{(30)}$$

Here:

M and N are two random events

$Prob\left(\frac{M}{N}\right)$ represents the probability of event M given event N is true or has already occurred

$Prob\left(\frac{N}{M}\right)$ represents the probability of event N given event M is true or has already occurred

$Prob\,(N)$ represents the individual probability of event N

$Prob\,(M)$ represents the individual probability of event M

Typically a regularization term σ is added so as to avoid the chances of overfitting by avoiding a strong bias for the weights updates. The proposed algorithm is explained subsequently.

Proposed Algorithm:
{
Start.
Step.1: Prepare labelled training vector for the classifier.

$$\boldsymbol{mse = \frac{1}{n}\sum_{i=1}^{n}(p_i - a_i)^2}$$

Where,
p **is the predicted value.**
a **is the actual value.**

Step. 2: Employ RGB-Grayscale conversion based on the relation:

$$I_{GS} = 0.28R + 0.5G + 0.09B$$

Step.3: Segmentation and CDR calculation:

Compute the radial gradient as:

$$g_r = \frac{\partial}{\partial r}\oint_{r,x_0,y_0}^{r,x_f,y_f} \frac{I(x,y)}{2\pi r} ds|$$

Compute: $argmin(P_T - P_C)$

$$if\ (argmin(P_T - P_C) \ll mean|P_S|$$

Replace patch with $mean|P_S|$

$$else$$

Replace patch with:

$$\frac{1}{n}(\sum_{i=1}^{n} \mu + \frac{\sigma^2}{(\sigma+1)^2}$$

Step.4: Compute the CDR value as:

$$CDR = \frac{radius\ of\ cup\ from\ origin}{radius\ of\ disc\ from\ origin}$$

Step.5: For illumination correction, compute the convolution of the Gaussian kernel and the original image bounded by the contour $'C'$**.**

$$for\ (i = 1\ to\ no.of\ scales)$$

{

$$I_R(x,y) = \sum_{i=1}^{n} w[I_O(x,y) * G(x,y)]\ \forall\ (x,y)\epsilon C$$

$$save\ matrix\ w_i$$

}

Step.6: Compute:

$$|kI - I_C|$$

Update the normalized 2-dimensional covariance matrix as:

$$C_{V-norm} = \frac{1}{m*n}\sum_{i=1}^{m}\sum_{j=i}^{n}(x_i - x_i')(x_i - x_i')$$

Step.7: Generate fused images as:

$$I_F = wC_{V-norm}I + I_C$$

Step.8: Decide decomposition levels $'n'$ **and family of wavelet function.**

Step.9: Compute the normalizing gradient as:

$$q(x,y) = \sqrt{\frac{c_1(\nabla I/_{I_F})^2 + c_2(\nabla^2 I/_{I_F})^2}{(1 + c_3(\nabla^2 I/_{I_F})^2}}$$

Step.10: $for\ i = 1{:}n$

$$retain\ C_A\ and\ discard\ C_D$$

Step.11: Compute the Normal and Cumulative Histograms of the original and de-noised images, along with the histogram metrics.

Step.12: Compute Feature Distribution over the entire range of image index.

Step.13: Initialize weights (w) randomly.

Step.14: Fix the maximum number of iterations (n).

Step.4: Define cost function as the mean squared error (mse) as:

Step. 15: Train the Network using the training rule:

$$w_{k+1} = w_k - \left[J_k J_k^T + \mu I\right]^{-1} J_k^T e_k$$

Step.16: Test network and compute accuracy.
Stop.
}

The performance of the proposed system is primarily computed in terms of the iterations to training convergence and the accuracy of the classifier. Less to moderate number of iterations imply that it would be practically feasible to implement the algorithm on hardware with processing power and memory constraints.
The performance metrics computed as:

The classification accuracy is computed as:

$$Ac = \frac{TP+TN}{TP+TN+FP+FN} \quad (31)$$

The sensitivity or recall is computed as:

$$Se\ or\ Re = \frac{TP}{TP+FN} \quad (32)$$

The precision is computed as:

$$Pr = \frac{TP}{TP+FP} \quad (33)$$

The specificity is computed as:

$$Sp = \frac{TN}{TN+FP} \quad (34)$$

Here,
(TP): True Positive
(TN): True Negative
(FP): False Positive
(FN): False Negative

1.Results

For the purpose of this study, 1000 images comprising of both positive and negative cases of glaucoma have been obtained from the Kaggle dataset [26]. The images acquired are .jpg images which three colour channels viz. R, G and B. The image enhancement and feature extraction has been performed on Matlab 2020a, with a RAM of 8GB and an i5-9300H CPU. All the images are first converted to common dimensions of (256 x 256). The features are then used to train a Deep Bayes Net with along with the typical CDR values. The performance metrics chosen are the accuracy of classification and prediction error in terms of the TP, TN, FP and FN values respectively. The results have been presented subsequently.

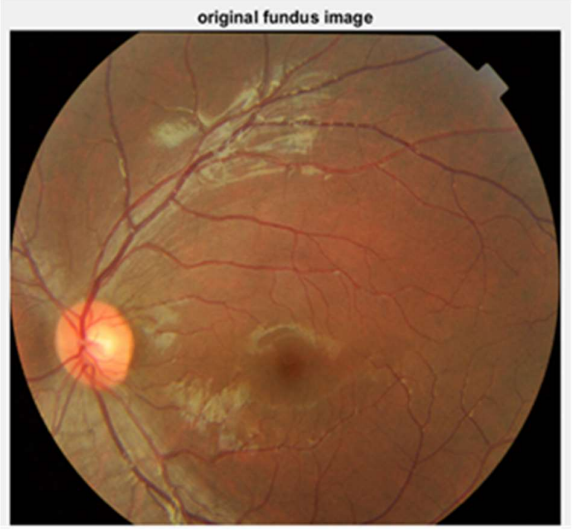

Figure 3 Original fundus image

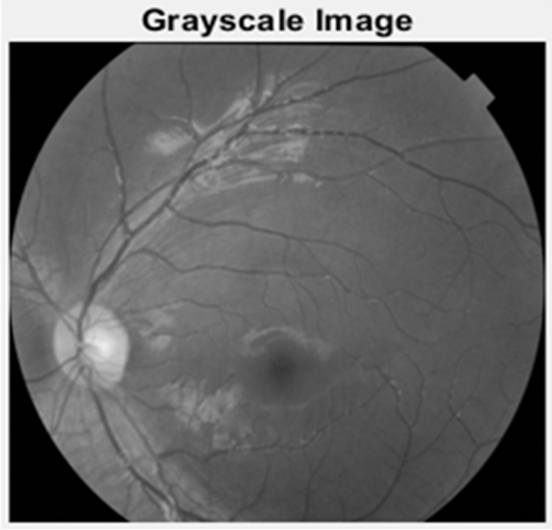

Figure 4 Grayscale Image

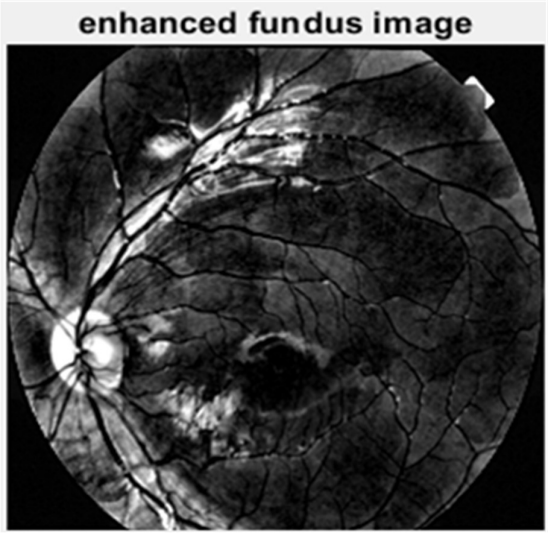

Figure 5 Enhanced image

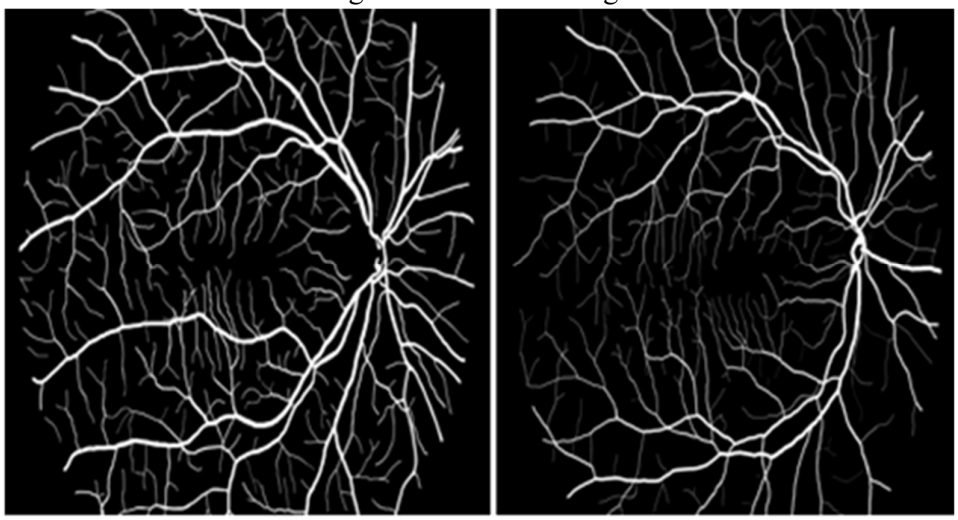

Figure 6 (a) Nerve Separation (Normal) (b) Nerve Separation (Glaucoma)

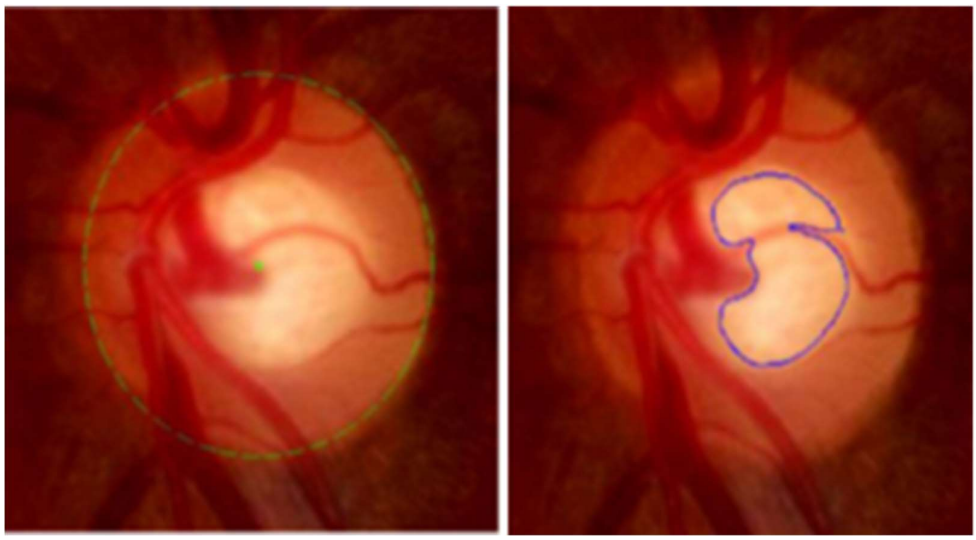

Figure 7 (a) Optical Disc Separated (b) Optical Cup Separated

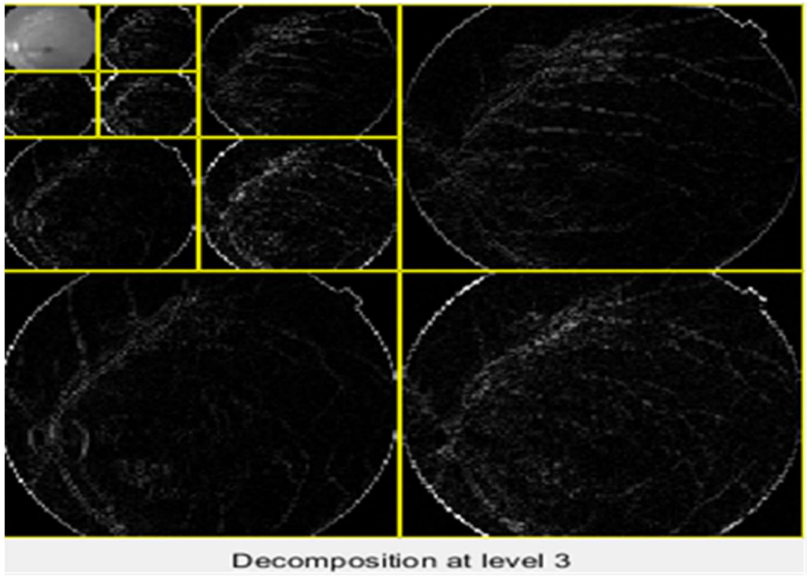

Figure 8Haarlet decomposition at level 3.

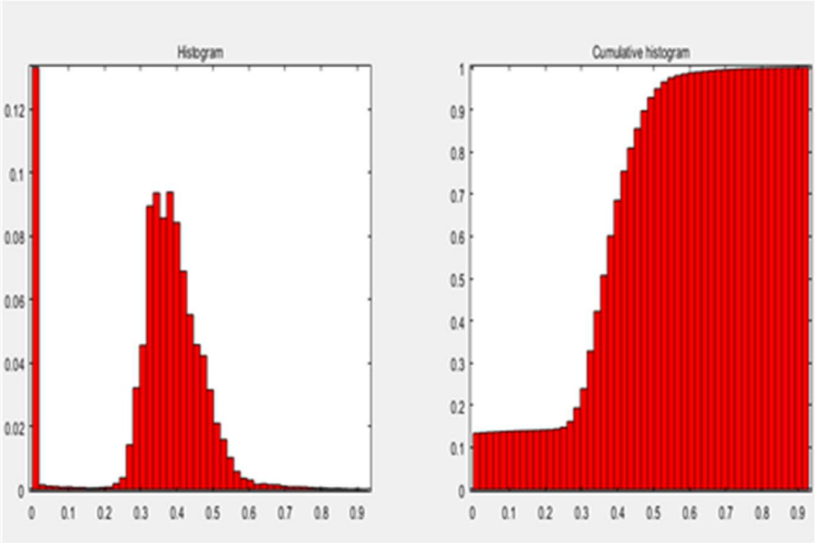

Figure 9Histogram Analysis of original image

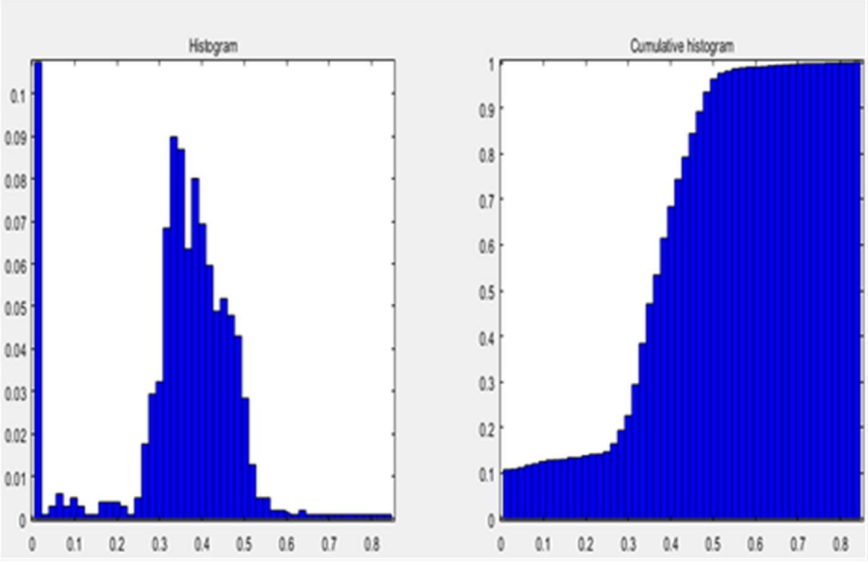

Figure 10Histogram Analysis of approximated image

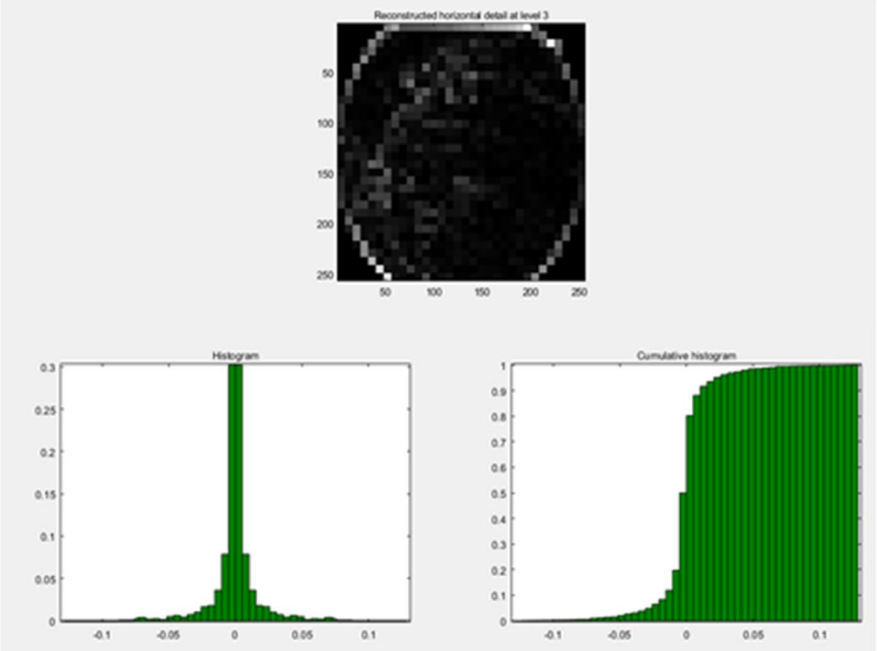

Figure 11Histogram Analysis of detailed co-efficients of image

Table 2Statistical parameters of the wavelet decomposition.

S.No.	Parameter	Values	Class
1.	Minimum	0	Original Image
2.	Maximum	0.9295	
3.	Mean	0.3415	
4.	Median	0.3703	
5.	Standard Deviation	0.1524	
6	Mean Absolute Deviation	0.05355	
7.	Minimum	0.002951	Approximate Co-efficient values
8.	Maximum	0.9165	
9.	Mean	0.3415	
10.	Median	0.3706	
11.	Standard Deviation	0.1511	
12.	Mean Absolute Deviation	0.05354	
13.	Minimum	-0.1592	Detailed Co-efficient values
14.	Maximum	0.1592	
15.	Mean	0	
16.	Median	0	
17.	Standard Deviation	0.01232	
18.	Mean Absolute Deviation	0.005539	

Table 3 Statistical Features

Features	Normal Fundus Image	Glaucoma Fundus Image

Contrast	0.362500000000000	0.328409090909091
Correlation	0.151836572326215	0.179081293145884
Energy	0.700218879132232	0.723267045454546
Homogeneity	0.915729166666667	0.921979166666667
Mean	0.00652645881744487	0.00227212218788613
Standard Deviation	0.106429183594269	0.106604988215597
Entropy	3.53356796596205	3.43675888527571
RMS	0.106600358177805	0.106600358177805
Variance	0.0111929089863435	0.0111892474804911
Smoothness	0.923435573787053	0.807650945366392
Kurtosis	6.63089615157184	6.70718347384146
Skewness	0.512491012022217	0.483428823467213

Figure 12Distribution of feature values

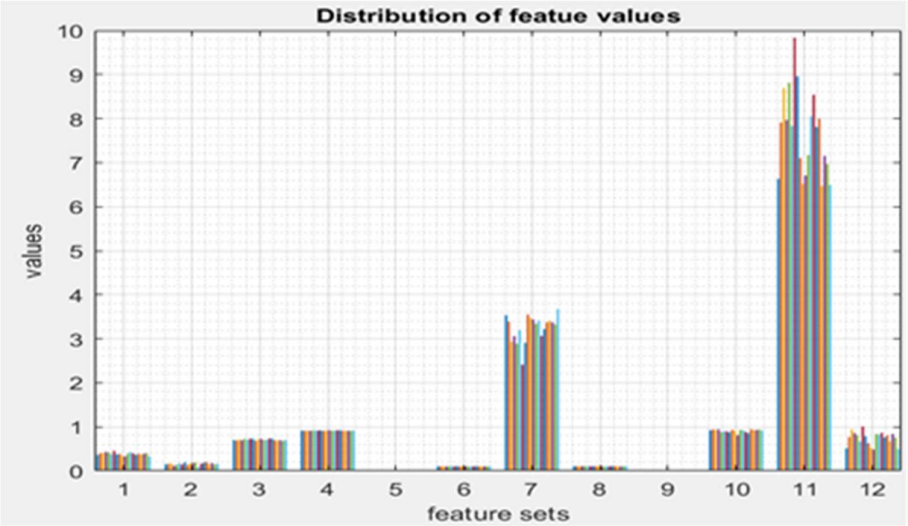

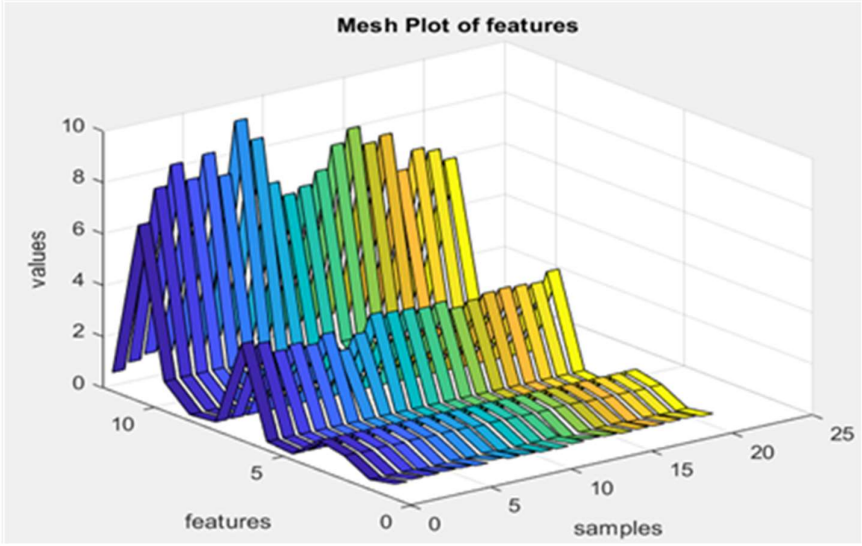

Figure 13Mesh Plot of features

Table.4Typical CDR values

Test Image	Normal Fundus Image	Glaucoma Fundus Image
1	0.486	0.628
2	0.482	0.592
3	0.458	0.648
4	0.620	0.588
5	0.581	0.575
6	0.501	0.680
7	0.562	0.695
8	0.591	0.578
9	0.510	0.640
10	0.595	0.655

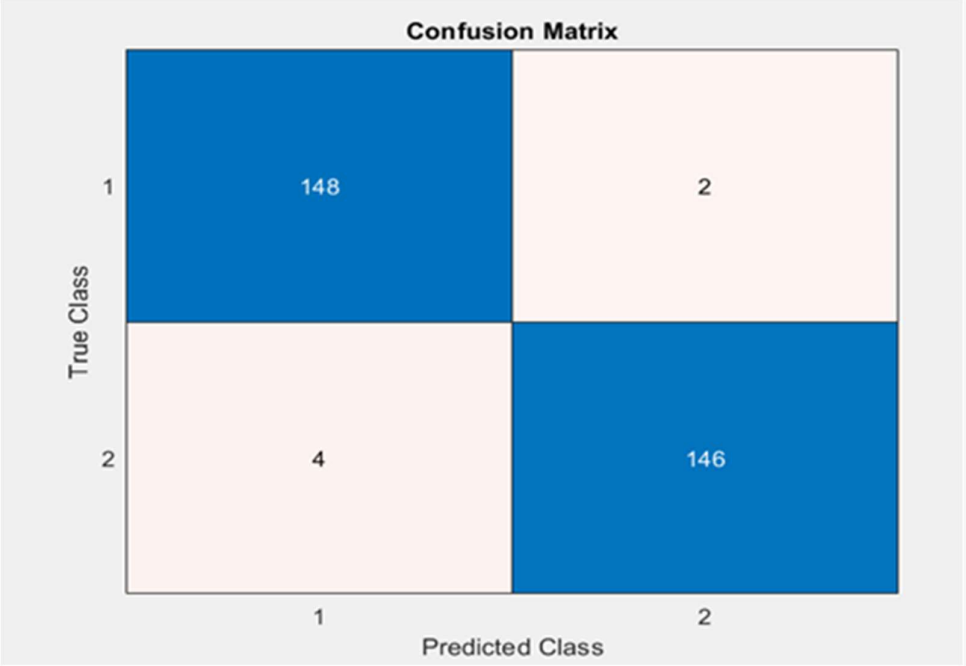

Figure 14Confusion Matrix

Table 5Performance Metrics

Parameter	Accuracy%	Sensitivity Or Recall%	Specificity%	Precision%
Value	0.980	0.9866	.9733	.9736

Table 6Comparative Analysis w.r.t. existing work

Method	Accuracy
Salam et al.	87%
Naik et al.	97.20
Sarkar et al.	97.58
Proposed	**98.0%**

Figure 3 depicts a sample fundus image which has been used for pre-processing and image enhancement followed by feature extraction. Figure 4 depicts the image after grayscale version of the image depicted in figure 3. Figure 5 depicts the background hue, saturation, values (HSV) estimation for the fundus image and subsequent image enhancement. The estimation of the HSV is helpful for image quality assessment (IQA) and facilitates the image enhancement process. The background normalization process helps to clearly identify the region under interest and further feature extraction.Figure 6 depicts the segmentation and separation of the optic nerves for the fundus images for both glaucoma positive and negative image. Figure 7 depicts the patch segmentation and identification of the optical cup and discs which later yields the CDR values.Figure 8 depicts the haarlet decomposition of the image at level 3. The choice of the haar wavelet family has been made due to the efficacy of the haarlet corresponding to image analysis. Sudden changes and spikes in image pixel values are filtered out using the 3rd

level decomposition. In the process, the approximate co-efficients are retained while discarding the detailed co-efficient of each level of decomposition. This allows the retaining maximum image information while discarding the noisy part of the image. The wavelet decomposition has been truncated to three levels to limit the system complexity. Increasing the decomposition levels beyond 5 has not shown significant improvement in image resolution based on the histogram analysis. The effectiveness of the recursive wavelet decomposition has been carried out based on the histogram analysis of the original and wavelet- processed images. Figure 9 depicts the normal and cumulative histogram of the original image. The normal and cumulative histograms clearly render the statistical features of the image in the transform domain (DWT-domain). Six critical statistical features in the transform domain have been chosen in this case for the analysis which are maximum value, minimum value, mean value, median, standard deviation and mean absolute deviation. Figures 10-11 depict the normal and cumulative histograms of the approximated image after retaining approximate co-efficents. The figure depicts the normal and cumulative histograms of the detailed or noisy image after retaining detailed co-efficents. The statistical co-efficients of the data are tabulated in table 1.

From table 2, it can be clearly seen detailed co-efficient values however tend to deviate from the actual data stream as the number of levels increase. This clearly indicates that if the approximate co-efficient values are retained and the detailed coefficient values are discarded, then the amount of local variations and noise can be removed. The wavelet transform can be used to maintain monotonicity in local intervals so as to make the training more effective for a classifier. The above argument indicates that the wavelet decomposition for feature extraction can enhance the accuracy of prediction and also increase the regression for large data sets. As an illustration, two separate fundus images have been analysed using the proposed algorithm and their features have been tabulated in table 3. It can be observed that the statistical feature values have identical values for both positive and negative cases of glaucoma, which necessitates the use of an accurate classifier. Table 4 tabulates the typical CDR values of normal and glaucoma affected image. It can be clearly observed that both positive and negative classes have overlapping values. Figure 12 depicts the distribution of the feature values of the images which implies that the features depict good correlation. Figure 13 depicts the mesh plot of the features. The plot can be used to visualize the variation in the feature values. A correlation among the distribution of the feature values can be seen from figures 12 and 13 which imply coherence in the results. Figure 14 depicts the confusion matrix of the proposed system which is an indicator of the accuracy of the system. Table 5 presents the performance metrics for the proposed algorithm.Table 6 presents a comparative study with respect to existing work in the domain. It can be observed from table 6 that the proposed work attains relative higher accuracy compared to existing methods in the domain.

5.Conclusion and future directions.

This paper presents a feature extraction and automated classification method for glaucoma using Discrete Wavelet Transform, GLCM features and the Deep Bayes Net with regularization. The purpose of the work is to design a low computational complexity based method for automated glaucoma detection which can be implemented practically on hardware constrained platforms as well. The recursive haarlet transform has been used for removal of noise and disturbances from the data. Statistical features along with the CDR values are

computed and used as the training vector to train the deep neural network. The Deep Bayes Net has been used as it serves as an effective classifier for overlapping boundary datasets. It has been shown that the proposed system attains a classification accuracy of 98% which is at par with existing work in the domain. Future enhancements of the work can be employing self-supervised (SSL) learning methods which would in turn reduce the time and effort in manual labelling of the datasets.

Conflicts of interest

The authors solemnly declare no conflict of interests.

References

1. Memari N, Ramli A, Saripan B, Mashohor S Moghbe M, 2019, Retinal Blood Vessel Segmentation by Using Matched Filtering and Fuzzy C-means Clustering with Integrated Level Set Method for Diabetic Retinopathy Assessment, Journal of Medical and Biological Engineering, 2019, 39, pp. 713–731.
2. Mendonca AM and Campilho, A. Segmentation of Retinal blood vessels by combining the detection of centre lines and morphological reconstruction, IEEE Transactions on Medical Imaging 2006, 25 (9): 1200-1213.
3. Perez P, Perez M, Perez M.E. and Arjona O, Parallel multiscale feature extraction and region growing: Application in retinal blood vessel detection, IEEE Transactions on Information Technology in Biomedicine 2020, 14(2): 500-506.
4. Marin D, Aquino A., Arias E., and Bravo M, A new supervised method for blood vessel segmentation in retinal images by using gray–level and moment invariants–based features", IEEE Transactions on Medical Imaging 2010, 30: 146-158.
5. Fraz M, Remagnino P., Hoppe A., Uyyanonvara B., Rudnicka A., Owen C., and Barman S. An ensemble classification–based approach applied to retinal blood vessel segmentation, IEEE Transactions on Biomedical Engineering 2012, 59: 2538-2548.
6. Xiao Z, Adel M. and Bourennane S., Bayesian method with spatial constraint for retinal vessel segmentation, Computational and Mathematical Methods in Medicine 2013, 13 (401413): 1-9.
7. Bansal N. and Dutta M. Retina vessels detection algorithm for biomedical symptoms diagnosis, International Journal of Computer Applications, 201371 (20):41-46.
8. Budai A., Bock R., Maier A., Hornegger J., and Michelson G.,Robust vessel segmentation in fundus images, International Journal of Biomedical Imaging, 2013 20: 1-11.
9. Wong D, Liu J, Tan N and Yin F, Automatic detection of the macula in retinal fundus images using seeded mode tracking approach, IEEE Annual International Conference of Engineering in Medicine and Biology Society (EMBC), 2012, 2: 4950-4953.
10. Khawaja A, Khan T, Khan M, and Nawaz S, 2019 A Multi-Scale Directional Line Detector for Retinal Vessel Segmentation, Sensors (Basel), 2019, 19 (22):4949.
11. Islam M, Wang J., Johnson S., Thurtell M., Kardon R and Garvin M, A Deep-Learning Approach for Automated OCT En-Face Retinal Vessel Segmentation in Cases of Optic Disc Swelling Using Multiple En-Face Images as Input, arvo journal 2020, 9 (2): 1-15.

12. Ceccon S, David F, Heath G, .David P Crabb and Tucker A., 2014 Exploring Early Glaucoma and the Visual Field Test: Classification and Clustering Using Bayesian Networks, IEEE Journal of Biomedical and Health Informatics, vol. 18, pp. 1008-1014.
13. DR Nayak, D Das, B Majhi, SV Bhandary, ECNet: An evolutionary convolutional network for automated glaucoma detection using fundus images, Biomedical Signal Processing and Control. Elsevier 2021, vol.67, pp. 102559
14. A Muacevic, J Adler, K Allison, D Patel, O Alabi, Epidemiology of Glaucoma: The Past, Present, and Predictions for the Future, Cureusvol.12, no.1 pp. 1-9.
15. Tham Y, Li X, Wong T, Quigley H, Aung T, Global prevalence of glaucoma and projections of glaucoma burden through 2040: a systematic review and meta-analysis, Ophthalmology, Elsevier 2014; 170 (11): 2081-2090.
16. Zaman F, Gieser S, Schwartz G, Swan C, A multicenter, open-label study of netarsudil for the reduction of elevated intraocular pressure in patients with open-angle glaucoma or ocular hypertension in a real-world setting, Current Medical Research and Opinion, Taylor and Francis, 2021, 37(6): 1011-1020.
17. Denis P, Duch S, Chen E, Klyve P, European real-world data about the use of a new delivery system containing a preservative-free multi-dose glaucoma treatment, European Journal of Ophthalmology, SAGE Publication 2021,31(3): 1056–1063.
18. Erb, C., Gast, U, Schremmer, D. German register for glaucoma patients with dry eye. I. Basic outcome with respect to dry eye. Graefe's Archive for Clinical and Experimental Ophthalmology, Springer 2008, 246:1593–1601.
19. Safdel, A., Hassani, K. Fluid–structure interaction analysis of alteration of the intraocular pressure on the optic nerve head in glaucoma. Journal of Optics, Springer 2021, 50:523–528.
20. Schwartz G, Patel A, Naik R, Lunacsek O, Characteristics and treatment patterns of newly diagnosed open-angle glaucoma patients in the United States: an administrative database analysis, Ophthalmology Glaucoma, Elsevier 2021, 4(2): 117-125.
21. Asaoka R, Murata H, Iwase A, Araie M, Detecting preperimetric glaucoma with standard automated perimetry using a deep learning classifier, Ophthalmology, Elsevier 2016, 123(9):1974-1980.
22. Suvarna H, Patil G, Automatic Glaucoma Detection Using CDR on Morphology and Hough Based Technique, 2018 International Conference on Electrical, Electronics, Communication, Computer, and Optimization Techniques (ICEECCOT), 2018, 954-96.
23. Fu H., Cheng J., Xu Y., Liu J. Glaucoma Detection Based on Deep Learning Network in Fundus Image. In: Lu L., Wang X., Carneiro G., Yang L. (eds) Deep Learning and Convolutional Neural Networks for Medical Imaging and Clinical Informatics. Advances in Computer Vision and Pattern Recognition. Springer, 2019: 119-137.
24. Salam A, Khalil T., Akram, M. et al. Automated detection of glaucoma using structural and non structural features. Springer Plus, 2016, 5:1519.
25. Ştefan A, Paraschiv E, Ovreiu S Ovreiu E, A Review of Glaucoma Detection from Digital Fundus Images using Machine Learning Techniques, International Conference on e-Health and Bioengineering (EHB), 2020:1-4.
26. Glaocoma Image Dataset, accessed from: https://www.kaggle.com/linchundan/fundusimage1000

27. Lim C, Lee C, Huang F, Huang J, Risk of Glaucoma in Patients Receiving Hemodialysis and Peritoneal Dialysis: A Nationwide Population-Based Cohort Study, International Journal of Environmental Research and Public Health, MDPI, 2020, 17(18):6774.
28. Sarkar D., Das S. Automated Glaucoma Detection of Medical Image Using Biogeography Based Optimization. In: Bhattacharya I., Chakrabarti S., Reehal H., Lakshminarayanan V. (eds) Advances in Optical Science and Engineering. Proceedings in Physics Springer, 2017, 194: 381-388.
29. Vijapur A., Kunte, R. Sensitized Glaucoma Detection Using a Unique Template Based Correlation Filter and Undecimated Isotropic Wavelet Transform. Journal of Medical and Biological Engineering, Springer 2017, 37:365–373.
30. Kumar K, Mishra R, Nandan D, Efficient Hardware of RGB to Gray Conversion Realized on FPGA and ASIC, Procedia Computer Science, Elsevier 2020, 171(2008):2015.
31. Cheng, K., Yu, Y., Zhou, H., GPU fast restoration of non-uniform illumination images. Journal of Real-Time Image Processing, Springer 2021, 18:75–83.
32. Elharrouss, O., Almaadeed, N., Al-Maadeed, S. Image Inpainting: A Review, Neural Process Letters, Springer 2020, 51:2007–2028.
33. Khmag, A., Ramli, A, Al-haddad S, Natural image noise level estimation based on local statistics for blind noise reduction. The Visual Computer, Springer 2018, 34: 575–587.
34. Choi H, Jeong J, Speckle noise reduction in ultrasound images using SRAD and guided filter, 2018 International Workshop on Advanced Image Technology (IWAIT),IEEE, 2018:1-4.
35. Dytso A, Vincent Poor H, Estimation in Poisson Noise: Properties of the Conditional Mean Estimator, IEEE Transactions on Information Theory, 2020, 66(7) :4304-4323.
36. Khmag, A., Haddad S., Ramlee R,. Natural image noise removal using non local means and hidden Markov models in stationary wavelet transform domain. Multimedia Tools and Applications, Springer 2018, 77:20065–20086.
37. Qin L, Wang Z, Guan Q, Guo X, Wang G, Variational Bayesian image restoration with multi-structured model of wavelet transform coefficients, Signal Processing: Image Communication, Elsevier, 72: 1-8.
38. He, L., Wang, Y., Xiang, Z. Wavelet frame-based image restoration using sparsity, nonlocal, and support prior of frame coefficients. The Visual Computer, Springer 2019, 35: 151–174 (2019).
39. Kimlyk M, Umnyashkin S, Image denoising using discrete wavelet transform and edge information, 2018 IEEE Conference of Russian Young Researchers in Electrical and Electronic Engineering (EIConRus), 2018: 1823-1825.
40. Singh L., Janghel R. Image Denoising Techniques: A Brief Survey. In: Yadav N., Yadav A., Bansal J., Deep K., Kim J. (eds) Harmony Search and Nature Inspired Optimization Algorithms. Advances in Intelligent Systems and Computing, Springer 2019, 741: 731-740.
41. Pal B., Bhateja V., Johri A., Pal D., Satapathy S. Glaucoma Detection Using Morphological Filters and GLCM Features. In: Satapathy S.C., Bhateja V., Favorskaya M.N., Adilakshmi T. (eds) Smart Computing Techniques and Applications. Smart Innovation, Systems and Technologies, Springer 2021, 224: 627-635.
42. Srivastava, D., Rajitha, B., Agarwal, S. Pattern-based image retrieval using GLCM. Neural Computing and Applications, Springer 2020, 32: 10819–10832

43. Khowaja, S., Khuwaja, P, Ismaili, I. A framework for retinal vessel segmentation from fundus images using hybrid feature set and hierarchical classification Signal,Image and Video Processing, Springer 2018, 13:379–387
44. Ursuleanu T, Luca A, Gheorghe L, Grigorovici R, Iancu S, Hlusneac M, Preda C, , Grigorovic A, Deep Learning Application for Analyzing of Constituents and Their Correlations in the Interpretations of Medical Images, Diagnostics, MDPI 2021, 11:1373.
45. Lyu W, Lu W, Ma M, No-reference quality metric for contrast-distorted image based on gradient domain and HSV space, Journal of Visual Communication and Image Representation, Elsevier 2020, 69:102797.
46. Chaudhary P, Pachori R, Automatic diagnosis of glaucoma using two-dimensional Fourier-Bessel series expansion based empirical wavelet transform, Biomedical Signal Processing and Control, Elsevier 2021, 64: 102237.
47. Srivastava D, Rajitha B, Agarwal S, Singh S. Pattern-based image retrieval using GLCM, Neural Computing and Applications, Springer 2020, 32:10819–10832.
48. Zhou W, Yu L, Qiu W, Zhou Y, Wu M. Local gradient patterns (LGP): An effective local-statistical-feature extraction scheme for no-reference image quality assessment, Information Sciences, Elsevier 2017, 397-398: 1-14.

49. Vlachas P, Pathak J, Hunt B, Sapsis T.P, Girvan M. Backpropagation algorithms and reservoir computing in recurrent neural networks for the forecasting of complex spatiotemporal dynamics, Neural Network, Elsevier 2020, 126:191-217.
50. I. Khan et al., Design of Neural Network With Levenberg-Marquardt and Bayesian Regularization Backpropagation for Solving Pantograph Delay Differential Equations, in IEEE Access, 2020, 8: 137918-137933.
51. Pei-Hung Chen, Wei Wei, Cho-Jui Hsieh, Bo Dai Proceedings of the 38th International Conference on Machine Learning, PMLR 2021 139:1760-1770.